

Article

# Effect of Preparation Method of Co-Ce Catalysts on CH<sub>4</sub> Combustion

Sofia Darda <sup>1,2</sup>, Eleni Pachatouridou <sup>1</sup>, Angelos Lappas <sup>1</sup> and Eleni Iliopoulou <sup>1,\*</sup>

<sup>1</sup> Chemical Process & Energy Resources Institute (CPERI), Centre for Research & Technology Hellas (CERTH), 6th km. Charilaou—Thermi Rd., Thermi, GR-57001 Thessaloniki, Greece; dardasofia@gmail.com (S.D.); e\_pahat@cperi.certh.gr (E.P.); angel@cperi.certh.gr (A.L.)

<sup>2</sup> Department of Chemical Engineering, Aristotle University of Thessaloniki, P.O. Box 1517, 54006 Thessaloniki, Greece

\* Correspondence: eh@cperi.certh.gr; Tel.: +30-2310-498312

Received: 21 January 2019; Accepted: 22 February 2019; Published: 27 February 2019



**Abstract:** Transition metal oxides have recently attracted considerable attention as candidate catalysts for the complete oxidation of methane, the main component of the natural gas, used in various industrial processes or as a fuel in turbines and vehicles. A series of novel Co-Ce mixed oxide catalysts were synthesized as an effort to enhance synergistic effects that could improve their redox behavior, oxygen storage ability and, thus, their activity in methane oxidation. The effect of synthesis method (hydrothermal or precipitation) and Co loading (0, 2, 5, and 15 wt.%) on the catalytic efficiency and stability of the derived materials was investigated. Use of hydrothermal synthesis results in the most efficient Co/CeO<sub>2</sub> catalysts, a fact related with their improved physicochemical properties, as compared with the materials prepared via precipitation. In particular, a CeO<sub>2</sub> support of smaller crystallite size and larger surface area seems to enhance the reducibility of the Co<sub>3</sub>O<sub>4</sub>/CeO<sub>2</sub> materials, as evidenced by the blue shift of the corresponding reduction peaks (H<sub>2</sub>-TPR, H<sub>2</sub>-Temperature Programmed Reduction). The limited methane oxidation activity over pure CeO<sub>2</sub> samples is significantly enhanced by Co incorporation and further improved by higher Co loadings. The optimum performance was observed over a 15 wt% Co/CeO<sub>2</sub> catalyst, which also presented sufficient tolerance to water presence.

**Keywords:** Co<sub>3</sub>O<sub>4</sub>; CeO<sub>2</sub>; complete CH<sub>4</sub> oxidation; hydrothermal synthesis; precipitation

## 1. Introduction

Today, CH<sub>4</sub>, N<sub>2</sub>O, and CO<sub>2</sub> emissions represent approximately 98% of the total greenhouse gas (GHG) inventory worldwide, a percentage expected to increase even further in the 21st century. Methane is the main compound of natural gas (NG) and is today used in various industrial processes and also as energy source in gas turbines or natural gas fuelled vehicles. Heavy-duty (HD) natural gas-fuelled fleet represents today less than 2% of the total fleet, however this percentage is expected to grow to represent as much as 50% in the near future. Moreover, methane is considered a substantially more potent greenhouse gas (GHG) than CO<sub>2</sub> and, hence, leakage of only a small percentage of methane from the supply chain could alter the net climate benefits of NG, which is lately suggested as an alternative fuel for heavy-duty (HD) transportation. Methane can be also a result of incomplete combustion processes, similarly to CO, while both of them are well-known environmentally detrimental pollutants and, thus, proper catalytic oxidation converters are needed for their abatement [1,2]. Noble metals and transition metals are the most commonly used components of such catalysts, investigated for methane and/or CO complete oxidation. Both these groups of catalysts have been extensively studied in order to develop efficient catalytic systems for combustion

of methane, recognized as the lowest reactivity molecule among alkanes. All up to date research efforts have disclosed the superiority of the noble metals (especially Pt, Pd, and their mixtures) on oxide supports [3–5]. However, there are many factors defining the effectiveness of these supported catalysts, including the nature and properties of the support, the metal loading, the size, shape, and electronic state of metal nanoparticles and their interaction/synergy with the support, their preparation method and, finally, any pretreatment conditions possibly applied for their improvement [6]. However, in spite of their excellent activity, their applications at a larger scale have been limited because of their prohibitively high cost, their shortage in worldwide reserves, and their prompt deactivation during methane oxidation, mainly due to sintering of supported noble metal nanoparticles [7]. On the other hand, transition metal oxides have recently attracted considerable attention as alternative catalytic materials, among which cobalt oxide is considered as the most promising catalyst for methane combustion. Most crucial property of the early transition metal oxides is the fact that they can generate oxygen vacancies, suggested as the necessary sites that can activate molecular oxygen for oxidation applications [5].  $\text{Co}_3\text{O}_4$  nanosheets are reported to show better catalytic activity than  $\text{Co}_3\text{O}_4$  nanobelts and nanocubes for  $\text{CH}_4$  oxidation, in spite of their low specific surface area.  $\text{Co}_3\text{O}_4$  catalysts with various structures (nanoparticles, two-dimensional and three-dimensional structures) were also investigated for methane catalytic combustion, exhibiting that enhanced catalytic performance of methane of the 2D- $\text{Co}_3\text{O}_4$  and 3D- $\text{Co}_3\text{O}_4$  catalysts is related with their noticeable reducibility and existence of abundant active  $\text{Co}^{3+}$  species [8,9]. Highly porous  $\text{Co}_3\text{O}_4$  nanorods, with narrow pore-size distribution and a high surface area were synthesized by simple hydrothermal methods and similarly exhibited an enhanced catalytic performance for  $\text{CH}_4$  oxidation, especially at high GHSV (Gas Hourly Space Velocity) conditions [10].  $\text{Co}_3\text{O}_4$  nanomaterials were also synthesized by hydrothermal method and tested for low temperature CO oxidation and methane combustion in another report. In that case, addition of ethylene glycol and its varying concentration significantly influenced the size and shape of the  $\text{Co}_3\text{O}_4$  oxides (resulting in nanosheets or nanospheres). During catalyst evaluation, it was evidenced that the  $\text{Co}_3\text{O}_4$  nanosheets exhibited more active oxygen species than the  $\text{Co}_3\text{O}_4$  nanospheres, a fact accounting for their higher activity in the oxidative reactions [11].

In addition to cobalt, several ceria-based, low-cost catalysts have recently attracted much attention as a reliever of costly, unstable noble metal catalysts, since they exhibit good performance in oxidation reactions of carbon monoxide and lower hydrocarbons. Once more, the synthesis method is very crucial; for example nanocrystalline  $\text{CeO}_2$ , as small as 5 nm, were prepared by the precipitation method, using hydrogen peroxide as an oxidizer and is reported to present even 100 °C lower methane oxidation temperature, as compared with microcrystalline  $\text{CeO}_2$ . Nabih et al. has also reported the synthesis of mesoporous ceria nanoparticles (NPs) by combining the sol-gel (SG) process with the inverse mini-emulsion technique. These materials were of high specific surface area and exhibited an even better catalytic performance than the reference samples, synthesized by precipitation [12,13]. The addition of  $\text{MO}_x$  (M: di- or tri-valent transition metal ion) in  $\text{CeO}_2$  is interestingly reported to promote the catalytic activity for the oxidation reaction, a fact possibly related with improved redox properties and high oxygen storage capacity, induced by the synergistic effect between  $\text{CeO}_2$  and  $\text{MO}_x$  [14–17]. A nanocomposite catalyst  $\text{Co}_3\text{O}_4/\text{CeO}_2$  is very recently reported to exhibit high activity in complete oxidation of  $\text{CH}_4$ , suggesting a synergistic effect of  $\text{CeO}_2$  nanorods and the supported  $\text{Co}_3\text{O}_4$  nanoparticles [7].

In addition to oxidation performance, catalyst tolerance to deactivation, caused by poisoning and thermal aging, is also a problem in all natural gas applications. Poisoning is either due to adsorption of impurities, e.g., S, P, Zn, Ca, and Mg, present in the exhaust gases, on the catalytic active sites or their reaction with the active sites causing the formation of non-active compounds. Sulfur in the NG vehicles exhaust gas actually originates from odorants and lubricating oils and less from gas itself. Sulfur is considered as the most noxious component readily deactivating Pd catalysts, recognized as the most efficient for methane oxidation. Only small amounts of  $\text{SO}_2$  can significantly inhibit catalyst activity by blocking the active noble metal sites by sulfur compounds [18–21]. Moreover,

water is always present in the process of the catalytic combustion of methane, either as gas humidity or as a combustion product. Water presence may affect the reaction kinetics, resulting in a serious inhibition of the oxidation reactions [14]. Thus, activity of Pd/Al<sub>2</sub>O<sub>3</sub> is reported as severely inhibited by water at temperatures below 450 °C, a fact attributed to the formation of surface hydroxyl groups, which blocks active catalyst sites, while suppressed oxygen exchange between support and PdO via the formed hydroxyl groups is another recent explanation. Based on experiments and kinetic modelling two are the suggested routes of the water inhibition effect; rapid adsorption of water species on the active sites and slow build-up of hydroxyl species. Formation of these surface hydroxyls is enhanced by high concentration of oxygen and high concentration of water vapor [22]. In general, while various mechanisms have been proposed in the literature to explain the deactivation observed due to water presence, all studies agree on a strong effect of the support. Thus, tuning opportunely the metal-support interaction and the oxygen exchange capability of the support is a suggested way to deal with water inhibition problem over Pd/CeO<sub>2</sub> catalysts, otherwise very highly active for methane oxidation in dry conditions [23]. In a recent study, Pt addition was suggested to improve the performance of Pd-modified Mn-hexaaluminate catalyst in the high-temperature oxidation of methane, especially in SO<sub>2</sub> and water presence, correlating the improved water and sulfur resistance with the presence of particles of PtPd alloy [24]. In a similar study, presence of water vapor is reported to significantly inhibit the catalytic performance of CeO<sub>2</sub>-MO<sub>x</sub> (M = Cu, Mn, Fe, Co, and Ni) mixed oxide catalysts for CH<sub>4</sub> combustion, while CeO<sub>2</sub>-NiO samples showed the best durability for CH<sub>4</sub> wet combustion (T50: 528 °C, when 20% water vapor was added in the reaction stream) among all materials tested [14]. Interestingly, water presence in the reaction feed is even reported to promote methane conversion over a NiO catalyst, prepared from thermal decomposition of the corresponding metal nitrate. As activation of oxygen plays a crucial role in methane oxidation, in the surface kinetics controlled region, the observed high catalytic efficiency of NiO is attributed to its larger capability for oxygen adsorption, even at 500 °C. The promoting role of water could be due to the fact that H<sub>2</sub>O molecules could modify the NiO surface and, thus, promote further activation of O<sub>2</sub> and/or CH<sub>4</sub> on the surface [25].

In a series of recent studies, we have investigated the impact of synthesis parameters on the solid state properties of CeO<sub>2</sub> materials. In detail, we followed four different, time- and cost-effective, preparation methods, i.e., thermal decomposition, precipitation, and hydrothermal method of low and high NaOH concentration, employing in all cases Ce(NO<sub>3</sub>)<sub>3</sub>·6H<sub>2</sub>O as the cerium precursor. A thorough characterization of all samples was carried out to gain insight into the impact of synthesis route on the textural, structural, morphological, and redox properties of the derived materials. The results revealed the superiority of the hydrothermal method towards the development of ceria nanoparticles of high specific surface area (>90 m<sup>2</sup> g<sup>-1</sup>), well-defined geometry (nanorods) and improved redox properties. Employing CO oxidation as a probe reaction evidenced a direct quantitative correlation between the catalytic activity and the abundance of easily reduced, loosely bound oxygen species. More specifically, the rod-like morphology of the hydrothermally synthesized CeO<sub>2</sub> nanoparticles, with well-defined (100) and (110) reactive planes, favored the enhanced reducibility and lattice oxygen mobility, rendering this material appropriate as catalyst or supporting carrier [26–28]. The current study aims in the preparation of novel Co-Ce catalytic materials targeting in the complete combustion of CH<sub>4</sub>. Co incorporation on an optimum selected CeO<sub>2</sub> support aims to promote the catalytic activity for the oxidation reactions, via an attempted improvement of the redox property and high oxygen storage capacity, deliberately induced by the synergistic effect between CeO<sub>2</sub> and CoO<sub>x</sub>. We purposely explored the effect of both the synthesis method of the CeO<sub>2</sub> support (following either the hydrothermal or precipitation technique) and the metal loading (0, 2, 5, and 15 wt% Co) on the catalytic performance and durability for complete methane oxidation. Deactivation studies were also performed examining tolerance of the optimum selected catalysts to thermal aging and presence of water vapor in the reaction feed (wet CH<sub>4</sub> combustion).

## 2. Results and Discussion

### 2.1. Catalyst Characterization

#### 2.1.1. Textural and Structural Characterization

The physicochemical properties of catalytic materials are presented in Table 1. As expected [26], the synthesis method of CeO<sub>2</sub> greatly affects the specific surface area, the pore volume and the average pore diameter of the carrier. In addition, the mean particle size of CeO<sub>2</sub> presents important differences between the two synthesis methods. Applying the hydrothermal method (CeO<sub>2</sub>-H), the formed ceria presents higher surface area (110.9 m<sup>2</sup>/g) and smaller CeO<sub>2</sub> crystallites (11.8 nm) than the precipitated ceria (CeO<sub>2</sub>-P), where the growing up of the ceria crystallites (18.6 nm) resulted in decreased surface area (49.5 m<sup>2</sup>/g). The effect of synthesis method on the crystallite size is probably related with slower rates of crystal migration and crystallites grow up, when following the hydrothermal synthesis method. Incorporation of cobalt, on both CeO<sub>2</sub> carriers, as well as the increase of its metal loading, affects the texture of the CeO<sub>2</sub> support, decreasing the specific surface area of the derived, CeO<sub>2</sub>-supported, Co catalysts. On the contrary, in the case of pure Co<sub>3</sub>O<sub>4</sub>, the different synthesis method does not appear to significantly affect the specific surface area. However, applying the hydrothermal method (Co<sub>3</sub>O<sub>4</sub>-H), the formed Co oxide presents lower pore volume and average pore diameter and similarly smaller Co<sub>3</sub>O<sub>4</sub> crystallites than Co<sub>3</sub>O<sub>4</sub>-P (33.3 nm as compared to 42.2 nm, respectively). Lower crystallite sizes (16.1–16.8 nm) of Co<sub>3</sub>O<sub>4</sub> nanomaterials, synthesized by hydrothermal method are reported in the recent literature, probably related with lower calcination temperature, thus limiting aggregation of Co<sub>3</sub>O<sub>4</sub> crystallites in the sample [11]. It is noteworthy that much smaller Co<sub>3</sub>O<sub>4</sub> crystallites are also formed on the CeO<sub>2</sub>-H rather than the CeO<sub>2</sub>-P support (16.0 as compared to 76.6 nm, respectively), when incorporating 15 wt% Co on either support via wet impregnation, a fact indicating synergetic effects between the CeO<sub>2</sub>-H support and the incorporated Co oxide.

**Table 1.** Physicochemical properties of catalytic materials.

Catalyst	Co (wt%)	S <sub>BET</sub> (m <sup>2</sup> /g)	Pore Volume (cm <sup>3</sup> /g)	Average Pore Diameter (nm)	Mean Particle Size (nm) <sup>1</sup>	
					CeO <sub>2</sub>	Co <sub>3</sub> O <sub>4</sub>
CeO <sub>2</sub> -P	-	49.5	0.06	5.2	18.6	-
CeO <sub>2</sub> -H	-	110.9	0.55	19.9	11.8	-
2Co/CeO <sub>2</sub> -P	2.1	43.3	0.06	5.8	16.3	-
2Co/CeO <sub>2</sub> -H	2.3	100.3	0.49	19.5	8.1	-
5Co/CeO <sub>2</sub> -P	5.1	39.6	0.05	5.3	20.5	-
5Co/CeO <sub>2</sub> -H	5.1	92.1	0.23	9.5	9.4	17.8
15Co/CeO <sub>2</sub> -P	14.6	38.8	0.09	9.3	16.2	76.6
15Co/CeO <sub>2</sub> -H	15.4	78.9	0.14	7.3	6.4	16.0
Co <sub>3</sub> O <sub>4</sub> -P	-	15.5	0.14	47.6	-	42.2
Co <sub>3</sub> O <sub>4</sub> -H	-	12.8	0.04	11.4	-	33.3

<sup>1</sup> Measured by XRD diffractograms using the Scherrer equation, at (2θ) 28.6°, 47.5° for CeO<sub>2</sub> and 31.3°, 36.9° for Co<sub>3</sub>O<sub>4</sub>.

Representative XRD (X-Ray Diffraction) patterns of bare CeO<sub>2</sub>, Co<sub>3</sub>O<sub>4</sub> and xCo/CeO<sub>2</sub> prepared with either the precipitation or the hydrothermal method, are shown in Figure 1a,b respectively. As expected, both samples of CeO<sub>2</sub> supports (CeO<sub>2</sub>-P and CeO<sub>2</sub>-H) exhibit characteristic peaks predominately located at 2θ: 28.6°, 33.1°, 47.5°, 56.36°, 59.1°, 69.4°, 76.9°, and 79.2° and have face centered cubic structure with the lattice parameters  $a = b = c = 5.411 \text{ \AA}$  and  $\alpha = \beta = \gamma = 90^\circ$  [29], which are also preserved in the Co-supported catalysts.

Bare Co oxides (Co<sub>3</sub>O<sub>4</sub>-P and Co<sub>3</sub>O<sub>4</sub>-H) show diffraction peaks at 2θ: 19.0°, 31.3°, 36.9°, 38.5°, 44.8°, 55.9°, 59.4°, and 65.2°, which are attributed to the cobalt oxide Co<sub>3</sub>O<sub>4</sub> and suggest that the cobalt precursor led to the formation of a face centered cubic unit cell of Co<sub>3</sub>O<sub>4</sub> (space group *Fd3m*) with a

spinel type structure after calcination [9,11]. At low Co loadings (2 wt.%), no diffraction peak related to  $\text{Co}_3\text{O}_4$  was observed, while increasing Co loading (to 5 wt.% and 15 wt.%) leads to the development of low intensity  $\text{Co}_3\text{O}_4$  peaks ( $2\theta$ :  $31.3^\circ$ ,  $36.9^\circ$ , and  $44.8^\circ$ ) for  $\text{Co}/\text{CeO}_2\text{-P}$  (Figure 1a) and  $\text{Co}/\text{CeO}_2\text{-H}$  (Figure 1b) catalytic materials, respectively.

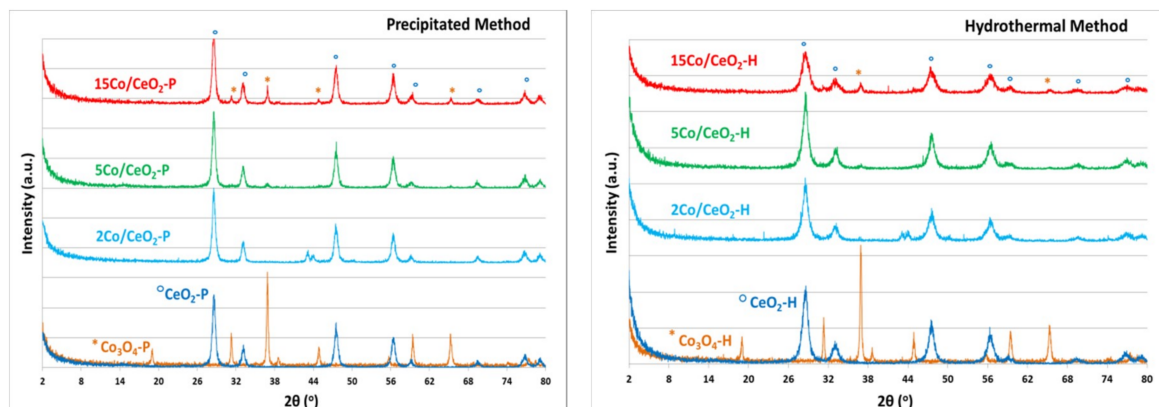


**Figure 1.** XRD patterns of  $\text{CeO}_2$ ,  $\text{Co}_3\text{O}_4$  and  $x\text{Co}/\text{CeO}_2$  prepared following the (a) precipitation method; and (b) the hydrothermal method. ( $x$ : 2, 5 or 15 wt% Co loading).

### 2.1.2. Morphological Characterization

The HR-TEM (High Resolution-Transmission Electron Microscopy) images further confirm the exposed planes of the two 15 wt.% Co catalysts, supported on differently synthesized  $\text{CeO}_2$  carriers. In both cases, two different face-centered cubic phases are identified, on taken electron diffraction patterns: a face-centered cubic phase of  $\text{CeO}_2$  with  $a = 0.541$  nm, and a second face-centered cubic phase of  $\text{Co}_3\text{O}_4$ , with  $a = 0.808$  nm. However, the morphology of the  $\text{Co}_3\text{O}_4/\text{CeO}_2$  catalysts is further explored with HR-TEM. In detail, low magnification images in Figure 2 (Figure 2a,b correspond to  $\text{CeO}_2\text{-P}$  and  $\text{CeO}_2\text{-H}$ , respectively) show an overview of the two catalytic samples. A very well defined, crystalline hexagonal formation (nanocrystalline structures of  $\text{CeO}_2$  are forming plates) is observed in the first case, while in the second case the  $\text{CeO}_2$  nanocrystals show a nanorod structure, an expected morphology related with the hydrothermal synthesis applied during ceria preparation [26]. Moreover, in both HR-TEM micrographs showing a very well defined hexagonal formation of  $\text{CeO}_2\text{-P}$  (Figure 2c), and a nanorod structure of  $\text{CeO}_2\text{-H}$  (Figure 2d) respectively, the characteristic d-spacings of the (111) planes are evidenced for both  $\text{CeO}_2$  supports, in agreement with the XRD patterns (characteristic peak, predominately located at  $2\theta$ :  $28.6^\circ$ ) [7].

As shown in Figure 3, both  $\text{CeO}_2$  nanocrystals and  $\text{Co}_3\text{O}_4$  nanoparticles are well crystallized, as evidenced by the clear lattice fringes in these HR-TEM micrographs. The coexistence of the  $\text{Co}_3\text{O}_4$  and  $\text{CeO}_2$  cubic phases is evidenced by fast Fourier transformation analysis (FFT). However,  $\text{Co}_3\text{O}_4$  nanoparticles are supported on bigger  $\text{CeO}_2$  nanocrystals with a size of about 25–30 nm (slightly larger than estimated via XRD patterns) over the  $\text{Co}/\text{CeO}_2\text{-P}$  sample (Figure 3a). The experimental lattice spacings of 0.285 nm and 0.243 nm, as well as the lattice spacings of 0.312 nm, can be assigned to (220) planes and (311) planes of the  $\text{Co}_3\text{O}_4$  cubic phase, and to the (111) planes of the  $\text{CeO}_2$  respectively. On the contrary, HR-TEM image of the  $\text{Co}/\text{CeO}_2\text{-H}$  sample (Figure 3b) shows a much smaller  $\text{CeO}_2$  nanorod (<20 nm), a trend in agreement with the XRD characterization. A smaller  $\text{Co}_3\text{O}_4$  nanoparticle with a size of about 15 nm, seems to be attached to these nanorod support. In this case, the experimental lattice spacings of 0.285 nm and 0.202 nm, as well as the lattice spacings of 0.312 nm, can be defined to (220) planes and (400) planes of the  $\text{Co}_3\text{O}_4$  cubic phase, and to the (111) planes of the  $\text{CeO}_2$ , respectively [7,9].

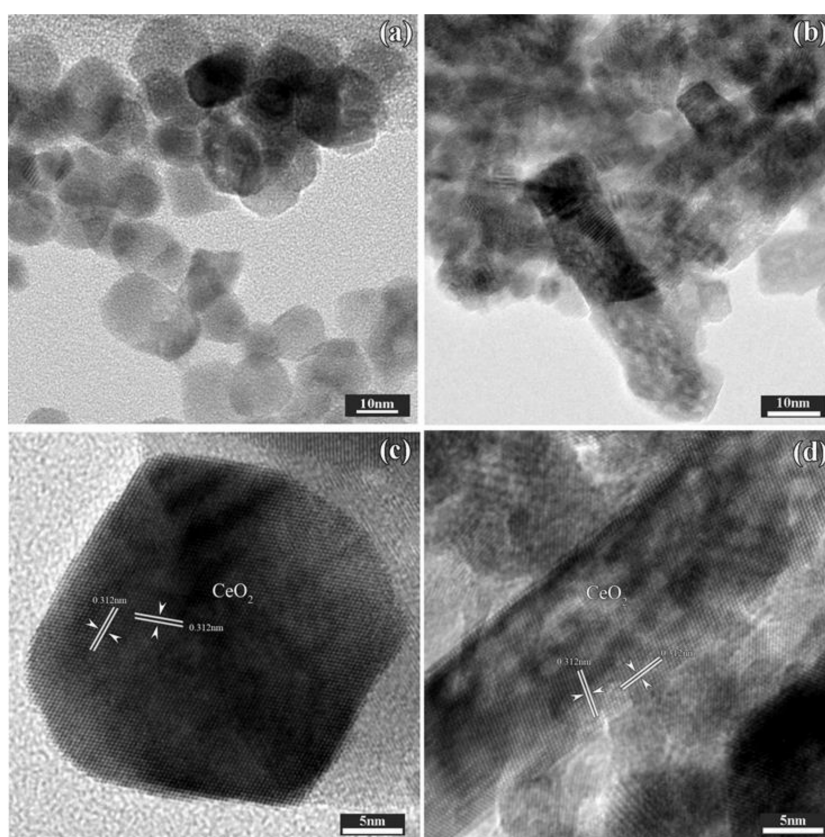


**Figure 2.** Low magnification images (overview) of the CeO<sub>2</sub> specimens, synthesized using the precipitation, CeO<sub>2</sub>-P (a) or the hydrothermal CeO<sub>2</sub>-H (b) method. The corresponding HR-TEM micrographs of the CeO<sub>2</sub>-P sample (c), and the CeO<sub>2</sub>-H sample (d), respectively.

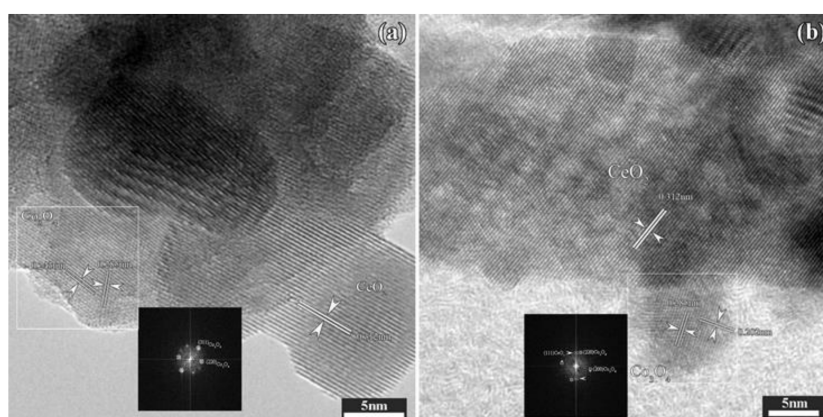


**Figure 3.** HR-TEM micrographs of the CeO<sub>2</sub>-P (a) and CeO<sub>2</sub>-H (b) specimens. As insets, FFT images taken at the white marked area are present for the two different cases, CeO<sub>2</sub>-P (a) and CeO<sub>2</sub>-H (b) samples, respectively.

### 2.1.3. H<sub>2</sub>-TPR and O<sub>2</sub>-TPD Studies

The reducibility of the catalysts was also investigated with H<sub>2</sub>-TPR experiments and the corresponding reduction profiles are presented in Figure 4. Bare CeO<sub>2</sub>-P and CeO<sub>2</sub>-H (Figure 4a,b insets, respectively) exhibit two peaks; one at 500–515 °C and one at 780–790 °C. The former is attributed to the reduction of surface oxygen of ceria, while the second one to the reduction of the bulk oxygen of CeO<sub>2</sub> [29,30]. Regarding pure Co oxides synthesized by different methods (Co<sub>3</sub>O<sub>4</sub>-P and Co<sub>3</sub>O<sub>4</sub>-H in Figure 4a,b insets, respectively), a broad double peak is observed in both cases, which is

associated with the reduction of  $\text{Co}_3\text{O}_4$  to  $\text{CoO}$  (T: 330–340 °C) and  $\text{CoO}$  to  $\text{Co}^0$  (T: 400–460 °C) [30,31]. It is worth to mention that for both materials prepared with hydrothermal method ( $\text{Co}_3\text{O}_4\text{-H}$  and  $\text{CeO}_2\text{-H}$ ) a blue shift is observed; the reduction peaks are shifted to lower temperatures, which indicates enhanced reducibility of both oxide materials under study.

Concerning the  $\text{H}_2$ -TPR profiles of  $x\text{Co}/\text{CeO}_2$  catalysts, all samples present three reduction peaks, which are also shifted to lower temperatures, in comparison with the corresponding bare  $\text{CeO}_2$  and  $\text{Co}_3\text{O}_4$  oxides (Figure 4a,b), an observation assigned to the interaction of Co with ceria. The first two peaks are related to the reduction of  $\text{Co}_3\text{O}_4$ , while the third one is attributed to the reduction of bulk oxygen of ceria support. In addition, the corresponding  $\text{H}_2$  consumption tends to increase as expected, as Co loading increases from 2 to 5, and finally to 15 wt. %.

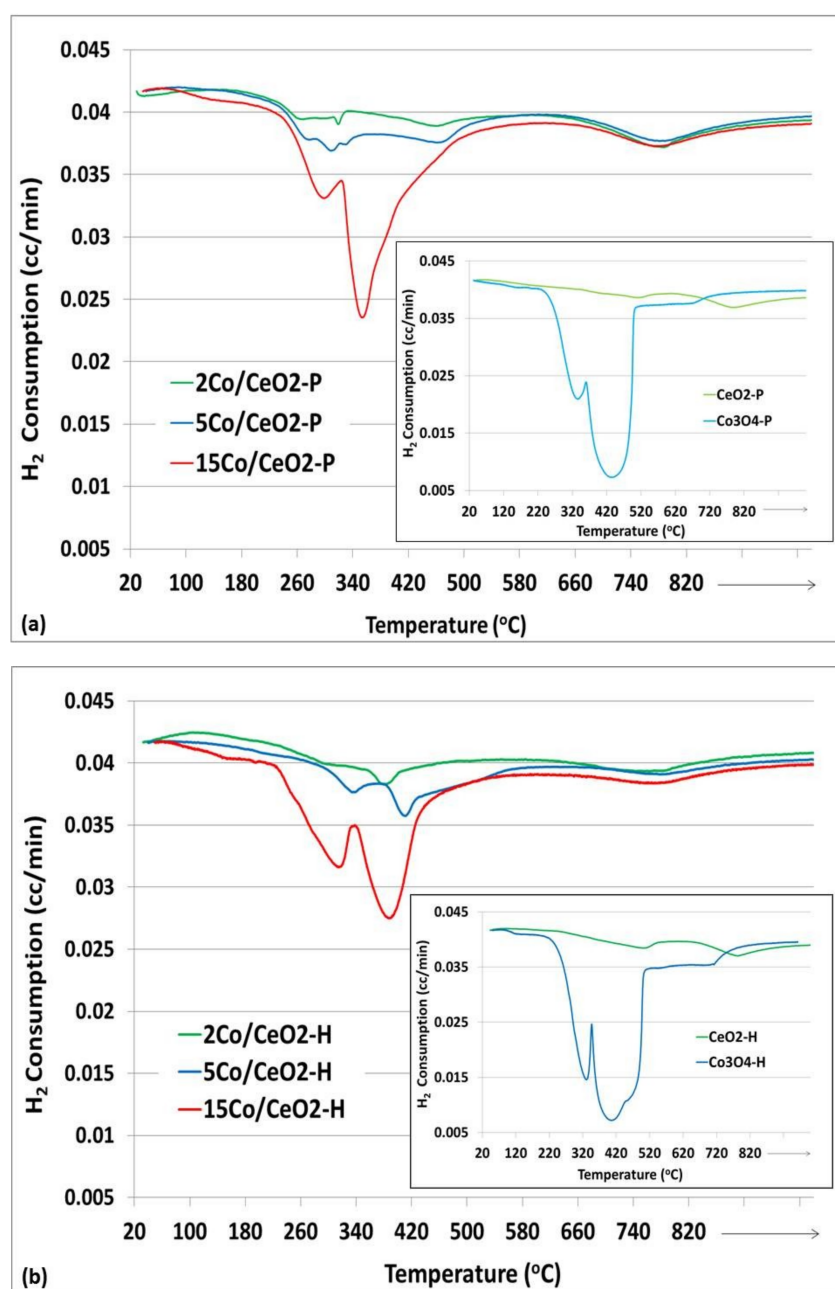


**Figure 4.** TPR profiles of bare  $\text{CeO}_2$ ,  $\text{Co}_3\text{O}_4$  (insets) and  $x\text{Co}/\text{CeO}_2$  catalysts prepared with: (a) Precipitation and (b) Hydrothermal Method. ( $x$ : 2, 5m or 15 wt% Co loading).

As suggested in several studies, during methane combustion the lattice oxygen in the oxide surface contributes to the oxidation of  $\text{CH}_x$ , thus leading to the formation of an oxygen vacancy, available for oxygen adsorption from the gas-phase. Both the adsorbed oxygen, as well as the surface lattice oxygen, are considered crucial for oxidation reactions, as they contribute to the adsorption/activation of oxygen and, thus, the desired oxidation of intermediates on the catalyst surface [11,32,33]. Oxygen-temperature programmed desorption ( $\text{O}_2$ -TPD) experiments have evidenced that oxygen molecules were released from  $\text{Co}_3\text{O}_4$  nanomaterials, suggesting that these oxygen molecules were adsorbed on the surface oxygen vacancies of the oxides [32]. These oxygen vacancies facilitate oxygen mobility of the oxide, forming the active oxygen species and, thus, enhancing the reaction activity with reductive molecules like  $\text{H}_2$  and  $\text{CH}_4$  [8,34]. Tuning the shape of the oxide catalyst, e.g. nanorods, nanocubes and nanosheets, is suggested to improve availability and abundance of these active oxygen species [26,35]. Especially, synthesis of  $\text{Co}_3\text{O}_4$  catalysts of specific shape in order to provide more active oxygen species in the catalyst surface is reported in the recent literature [11].

Figure 5 shows the profiles of  $\text{O}_2$  temperature-programmed desorption ( $\text{O}_2$ -TPD) of bare  $\text{CeO}_2$  (prepared either following the precipitation or the hydrothermal method) and the corresponding 15 wt.%  $\text{Co}/\text{CeO}_2$  supported catalysts. The bare ceria supports exhibit one peak at  $418^\circ\text{C}$ , related with the adsorbed atomic oxygen evolved from the bulk of  $\text{CeO}_2$  support [36]. The incorporation of 15 wt.%  $\text{Co}$  to  $\text{CeO}_2$  carriers shifted the peak to lower temperatures, suggesting that  $\text{O}_2$  desorption is facilitated, especially for the  $15\text{Co}/\text{CeO}_2\text{-H}$  catalyst (observed shift from  $418$  to  $376^\circ\text{C}$ ) [30]. In addition, both  $\text{Co}$ -based catalysts exhibit two extra peaks at a higher temperature area ( $500\text{--}650^\circ\text{C}$ ), which are related with the oxygen desorption from the surface of the  $\text{Co}$  oxides, while the peak observed at  $T > 700^\circ\text{C}$  corresponds to  $\text{O}_2$  desorption from the bulk of  $\text{Co}_3\text{O}_4$  [11].

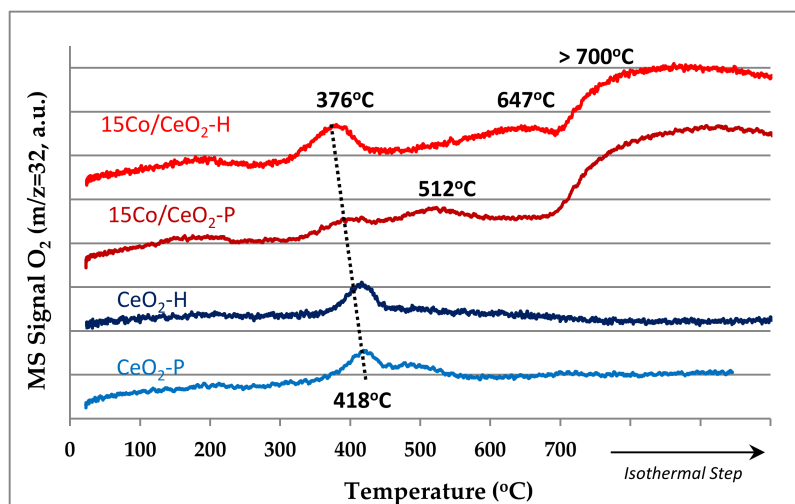


**Figure 5.**  $\text{O}_2$ -TPD profiles of the two bare  $\text{CeO}_2$  supports (prepared with either the precipitation or the hydrothermal method) and the corresponding 15 wt.%  $\text{Co}/\text{CeO}_2$  supported catalysts.

## 2.2. Catalytic Activity of Pure $\text{CeO}_2$ , Pure $\text{Co}_3\text{O}_4$ and $\text{Co}_3\text{O}_4/\text{CeO}_2$ Oxides for Methane Oxidation

The catalytic performances of all materials (pure  $\text{CeO}_2$ , pure  $\text{Co}_3\text{O}_4$  and  $\text{Co}_3\text{O}_4/\text{CeO}_2$  composite catalysts) in complete oxidation of methane were investigated using a fixed-bed reactor and are presented in Figure 6a. Below  $500^\circ\text{C}$ ,  $\text{CH}_4$  conversion was  $<10\%$  for pure  $\text{CeO}_2$  supports, while the  $\text{CeO}_2$  nanorods ( $\text{CeO}_2\text{-H}$ ) exhibit a slightly improved performance, finally reaching 41% conversion at  $600^\circ\text{C}$  (as compared to 31% conversion achieved with the  $\text{CeO}_2\text{-P}$  sample, respectively).  $\text{Co}$  incorporation via deposition of  $\text{Co}_3\text{O}_4$  nanoparticles on both  $\text{CeO}_2$  supports largely increased their catalytic activity for  $\text{CH}_4$  combustion, which is further enhanced as  $\text{Co}$  loading increases from 2 to 5 and, finally, 15 wt.%. However, an improved catalytic performance is always observed on the  $\text{CeO}_2\text{-H}$  (ceria nanorods) supported materials.  $\text{Co}$  incorporation on  $\text{CeO}_2$  nanorods achieves 10%  $\text{CH}_4$  conversion

from 420 °C and finally reaches up to ~90% CH<sub>4</sub> conversion at 600 °C (15Co/CeO<sub>2</sub>-H sample). It is worth to mention that on higher Co loadings (5 and 15 wt.%) a significant improvement (>15% higher conversion) is always observed, when using the CeO<sub>2</sub> nanorods support. This is probably related with the optimized physicochemical properties of this CeO<sub>2</sub>-H support: smaller CeO<sub>2</sub> crystallites, combined with higher surface area and possibly some synergetic effects between the deposited Co<sub>3</sub>O<sub>4</sub> and the CeO<sub>2</sub> carrier. These catalysts exhibit similar performance ( $T_{50\%} = 520$  °C) with materials reported in the recent literature [7], evaluated however at milder conditions (lower GHSV:18,000 h<sup>-1</sup> and different feedstock ~6.67% CH<sub>4</sub> and ~33.3% O<sub>2</sub>). Efficiency at high GHSV feeds is very important and still remains a significant challenge, as reported in the literature [10].

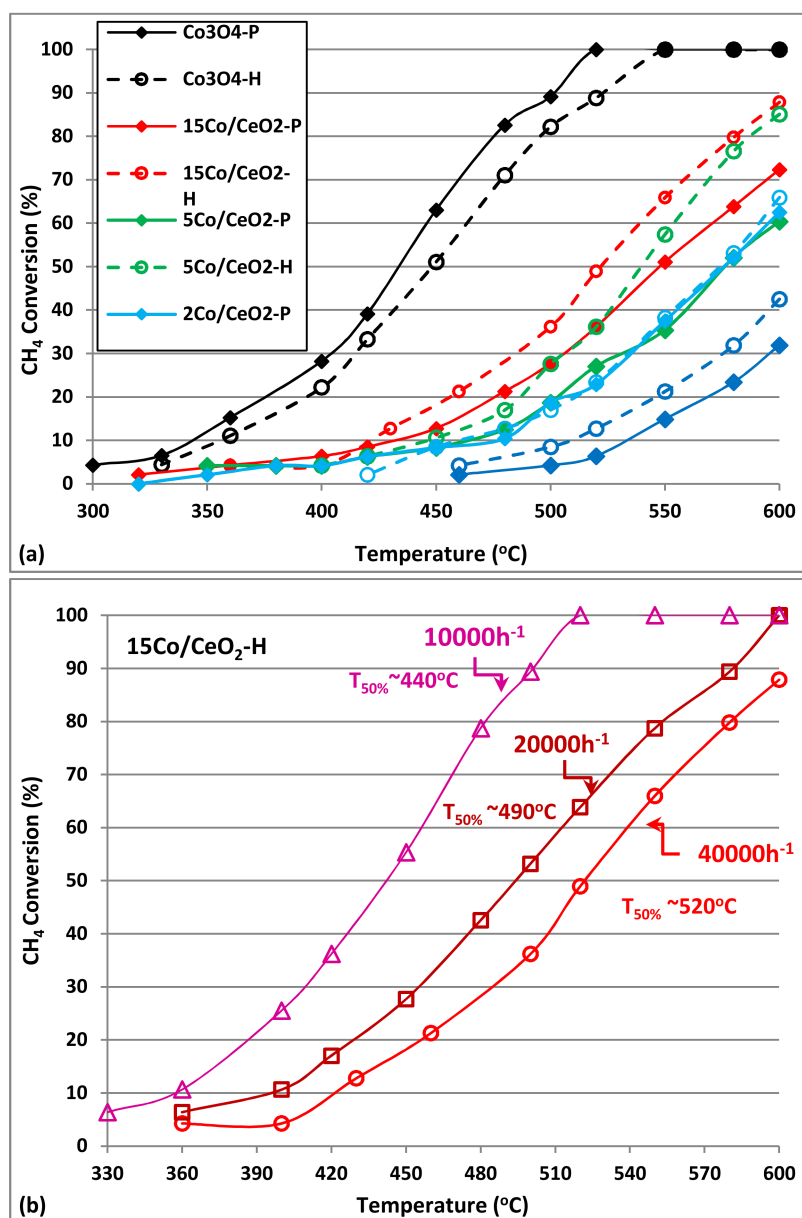


**Figure 6.** Catalytic performance in complete CH<sub>4</sub> oxidation on pure CeO<sub>2</sub>, Co<sub>3</sub>O<sub>4</sub> and nanocomposite Co/CeO<sub>2</sub> catalysts. (a) CH<sub>4</sub> conversion vs. temperature Flow rate: 900 cm<sup>3</sup>/min; GHSV~40,000 h<sup>-1</sup>; (b) Effect of WHSV on CH<sub>4</sub> conversion for the optimum selected 15Co/CeO<sub>2</sub>-H catalyst. Feed: 0.5% vol. CH<sub>4</sub> and 10% vol. O<sub>2</sub>, balanced with He.

In order to further exhibit superiority of our optimum material, 15Co/CeO<sub>2</sub>-H was further evaluated differentiating the reaction conditions used; varying GHSV between 10,000, 20,000, and 40,000 h<sup>-1</sup> (Figure 6b). As expected, 15Co/CeO<sub>2</sub>-H catalyst exhibits a significantly improved performance at lower GHSV reaching T<sub>50%</sub> = 440 °C, which is obviously much better when compared with similar reported catalysts (Co<sub>3</sub>O<sub>4</sub>/CeO<sub>2</sub> exhibiting T<sub>50%</sub> = 475 °C at WHSV of 9000 mL g<sup>-1</sup> h<sup>-1</sup>) [7]. Moreover, the much lower temperature for 50% conversion of CH<sub>4</sub> (T<sub>50%</sub>) on Co<sub>3</sub>O<sub>4</sub>/CeO<sub>2</sub>-H, as compared with the bare CeO<sub>2</sub>-H support (T<sub>50%</sub> = 440 °C as compared with T<sub>50%</sub> = 575 °C, respectively, at low GHSV: 10,000 h<sup>-1</sup> conditions), once more supports the significant role of the loaded Co<sub>3</sub>O<sub>4</sub> nanoparticles for complete oxidation of methane. Finally, the superior performance of pure Co<sub>3</sub>O<sub>4</sub> catalysts is very interesting, as these materials reached complete (100%) oxidation of CH<sub>4</sub> from 520 °C independently of their synthesis method and thus deserve further investigation.

### 2.3. Catalyst Stability Tests

Thermal stability of a catalyst used in the CH<sub>4</sub> catalytic combustion is very important because of its expected operation at high temperatures. In general, thermal aging may cause crystal growth and loss of catalytic surface. Thus, catalyst stability over time of the optimum selected material (15Co/CeO<sub>2</sub>-H) was tested under the flow of mixture of 0.5 vol% CH<sub>4</sub> and 10 vol% O<sub>2</sub>, balanced with He. As shown in Figure 7, the conversion at 600 °C is rather stable (only a small decrease from 88 to 81% is observed) after 10 hours on stream, under a GHSV of 40,000 h<sup>-1</sup>. This is probably attributed to the thermal stability of the particular oxides (CeO<sub>2</sub> and Co<sub>3</sub>O<sub>4</sub>), which are expected to deteriorate at higher operating windows (700–750 °C). Preservation of finely dispersed Co<sub>3</sub>O<sub>4</sub>/CeO<sub>2</sub> species after aging at 750 °C is reported to retain high methane oxidation activity and tolerance to thermal ageing, suggesting once more the importance of the preparation method to achieve intimate contact between the cobalt–ceria species leading to good oxidation activity [17].

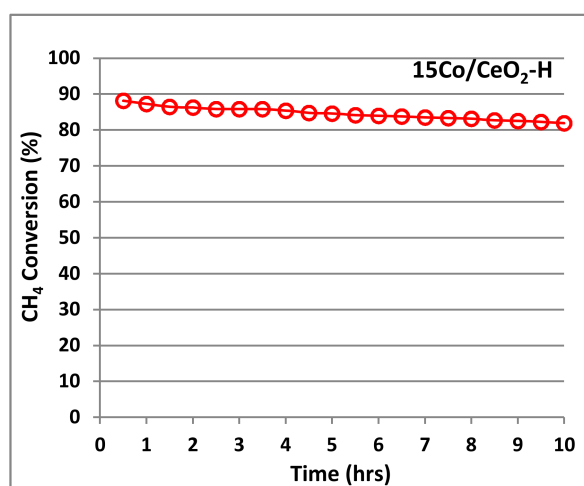


**Figure 7.** Response of CH<sub>4</sub> combustion to long-term stability tests over the optimum selected 15Co/CeO<sub>2</sub>-H catalyst; Flow rate: 900 cm<sup>3</sup>/min; GHSV~40,000 h<sup>-1</sup>; Reaction temperature 600 °C; Feed: 0.5% vol. CH<sub>4</sub> and 10% vol. O<sub>2</sub>, balanced with He.

The presence of ~10 vol.% of water in the NG exhausts still remains one of the main challenges for the required catalytic system to control the emissions of NG vehicles. Thus, in order to further test the water vapor effect on the catalytic performance of our optimum catalyst (15Co/CeO<sub>2</sub>-H) for methane oxidation, 5% and 10% water vapor was added in the process of CH<sub>4</sub> combustion and the corresponding catalytic performance is shown in Figure 8 in comparison with the case using the dry reaction gas. The amount of water added significantly exceeds the stoichiometric amount produced during combustion, under the conditions used in this work (0.5% CH<sub>4</sub>, 10% O<sub>2</sub>). Increasing the water

vapor content in the reaction stream, slightly descends its catalytic performance, as  $T_{50\%}$  is increased from 520 to 530 °C, when water vapor is added, while increase of water content (from 5 to 10 wt.%) does not induce any further inhibition effect. Thus, water presence does not lead to a significant activity fall (observed increase in  $T_{50\%}$  is less than 20 °C), while water effect is even more limited at higher temperatures of methane combustion. On the contrary, effect of water presence is most evident on the initiation temperature of the  $\text{CH}_4$  combustion, increasing  $T_{10}$  value from 420 to 450 °C [14]. Removing water from the reaction feed completely restored the initial activity of the catalyst, without the need to subject the catalyst to any regeneration/thermal treatment. The restored catalyst efficiency of the used catalyst suggests that the limited water inhibition effect is probably related with adsorption of water species on the active sites at the low temperature range. There is no evidence of hydroxyl species' build-up or sintering of Co species, which could lead to a more severe/permanent deactivation, in spite the high concentration of oxygen (10 wt%) and high concentration of water vapor (10 wt%) used, expected to facilitate formation of surface hydroxyls [22]. The steam reforming reaction of methane might be involved, during the  $\text{CH}_4$  catalytic combustion in the presence of water vapor, in which  $\text{CH}_4$  is partially oxidized to CO and  $\text{H}_2$ . However, analysis of the effluent gas hardly detected any CO, confirming that  $\text{CH}_4$  is totally oxidized to  $\text{CO}_2$  and  $\text{H}_2\text{O}$  over 15Co/CeO<sub>2</sub>-H, even in the presence of water vapor (wet  $\text{CH}_4$  catalytic combustion).

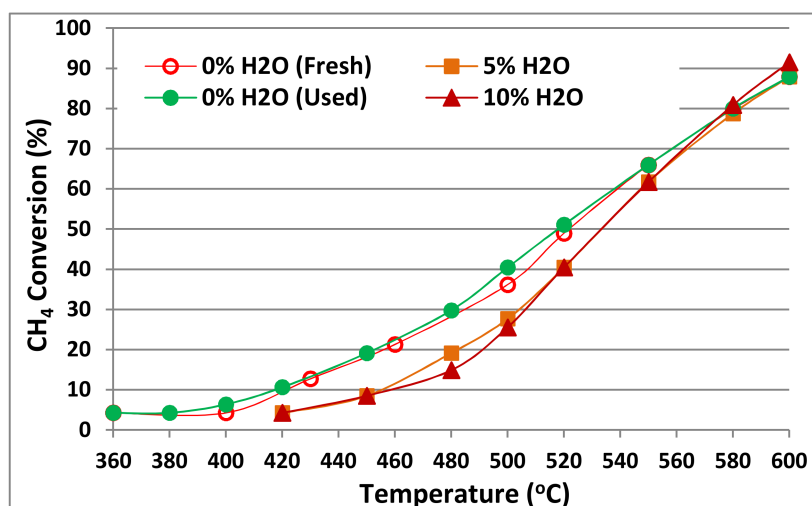


**Figure 8.**  $\text{CH}_4$  catalytic combustion over 15Co/CeO<sub>2</sub>-H (fresh and used) with different contents of water vapor addition (0, 5 and 10 wt%). Flow rate: 900 cm<sup>3</sup>/min; GHSV~40,000 h<sup>-1</sup>.

### 3. Materials and Methods

The CeO<sub>2</sub> carrier was prepared with two different methods; the precipitation method (CeO<sub>2</sub>-P) and the hydrothermal method (CeO<sub>2</sub>-H). Cerium nitrate hexahydrate (Ce(NO<sub>3</sub>)<sub>3</sub>·6H<sub>2</sub>O, 99% purity, supplied by Fluka, Steinheim, Germany) was used as a precursor salt for both synthesis methods. For the final production of 25 g of CeO<sub>2</sub>-P we initially prepared an aqueous solution (0.5 M) of cerium nitrate dissolving ~63 g of Ce(NO<sub>3</sub>)<sub>3</sub>·6H<sub>2</sub>O in 290 mL of double distilled water. Then a precipitating agent (25 vol% NH<sub>3</sub> solution) was added at room temperature to the continuously stirred solution of the cerium nitrate, until the pH of the solution reached the value of 10. Then the pH remained stable at this value for additional 3 h. Following precipitation, the resulting precipitate was filtered, dried overnight at 110 °C and then calcined at 500 °C for 5 h under air flow. For the preparation of CeO<sub>2</sub>-H, 0.023 mol of cerium nitrate was dissolved in 46 mL of double distilled water. Then, 125 mL of a 1 M NaOH solution was added rapidly under vigorous stirring. The mixed solution was placed in a 1 L Teflon bottle, which was sealed and placed in an oven at 110 °C for 5 h. The as-obtained material was washed several times with double distilled water and ethanol, and then dried and calcined, following the same thermal treatment with the precipitated one.

The incorporation of cobalt over the CeO<sub>2</sub> supports was conducted by applying the incipient wetness impregnation method. A series of Co catalysts supported on CeO<sub>2</sub>-P and CeO<sub>2</sub>-H, were prepared in three different metal loadings (2, 5 and 15 wt%). Incorporation of the Co active phase was accomplished by using Co(NO<sub>3</sub>)<sub>2</sub>·6H<sub>2</sub>O (99% purity, supplied by Merck, Darmstadt, Germany). Aqueous solution of the metal salt was impregnated on CeO<sub>2</sub> supports, in successive stages, with intermediate drying in an oven at 100 °C for 30 min. The derived samples were dried at 110 °C overnight and finally calcined under air flow at 500 °C for 5 h. The as prepared composites are herein labeled as xCo/CeO<sub>2</sub>-P or H, where x is the cobalt loading.

For comparison reasons, bare Co<sub>3</sub>O<sub>4</sub> was prepared by precipitation (Co<sub>3</sub>O<sub>4</sub>-P) and hydrothermal (Co<sub>3</sub>O<sub>4</sub>-H) method. Co(NO<sub>3</sub>)<sub>2</sub>·6H<sub>2</sub>O was used as a precursor salt and the same precipitation method was followed as for the synthesis of CeO<sub>2</sub>-P. For the preparation of Co<sub>3</sub>O<sub>4</sub>-H, 0.0515 mol of cobalt nitrate was dissolved in 51 mL of double distilled water and 125 mL of a 1 M NaOH solution was added rapidly under vigorous stirring. Then, the next steps (aging, washing, and thermal treatment) were the same with the hydrothermal synthesis of ceria.

The physicochemical characteristics of as-synthesized materials were evaluated by various complimentary techniques. The total Co loading (wt%) of the final catalysts was determined by the Inductively Coupled Plasma Atomic Emission Spectroscopy (ICP-AES -on a Perkin-Elmer Optima 4300DV apparatus, Waltham, MA, USA). The textural characteristics of the as prepared catalysts were determined by the N<sub>2</sub> adsorption–desorption isotherms at −196 °C (Nova 2200e Quantachrome flow apparatus, Boynton Beach, FL, USA). Specific surface areas (m<sup>2</sup>g<sup>−1</sup>) were obtained according to the Brunauer-Emmett-Teller (BET) method at relative pressures in the 0.05–0.30 range. The specific pore volume (cm<sup>3</sup>g<sup>−1</sup>) was calculated based on the highest relative pressure, whereas the average pore size diameter (dp, nm) was determined by the Barrett-Joyner-Halenda (BJH) method. Prior to measurements the samples were degassed at 250 °C under vacuum. The crystalline structure of the catalysts was determined by powder X-ray diffraction (XRD) on a Siemens D 500 diffractometer (Bruker, Karlsruhe, Germany) operated at 40 kV and 30 mA with Cu Kα radiation (λ = 0.154 nm). Diffractograms were recorded in the 5–80° 2θ range and at a scanning rate of 0.02° s<sup>−1</sup>. The Scherrer equation was employed to determine the primary particle size of a given crystal phase based on the most intense diffraction peaks of CeO<sub>2</sub> (28.6°, 47.5°) and Co<sub>3</sub>O<sub>4</sub> (31.3°, 36.9°). The size, morphology and structure of the two 15 wt% Co-supported catalysts (either on CeO<sub>2</sub>-H or CeO<sub>2</sub>-P supports) were also investigated by transmission electron microscopy using a (JEOL JEM 2011 TEM, Zaventem, Belgium) operating at 200 kV with an atomic resolution of 0.194nm. The HR-TEM micrographs were analyzed using Digital Micrograph v2 software (Gatan, Inc., München, Germany).

Hydrogen temperature-programmed reduction (H<sub>2</sub>-TPR) experiments were performed in a different bench-scale unit, also available in our facilities for TPX studies, loading a fixed bed tubular reactor with 0.1 g of sample, while the reactor exit was coupled with a mass spectrometer (MS). A flow (50 cm<sup>3</sup>/min) of 5 vol% H<sub>2</sub>/He gas mixtures was used, while the temperature of the solid catalyst was increased to 800°C at the rate of 10 °C/min. The effluent gas from the reactor was analysed using the MS detector (m/z = 2 was used for H<sub>2</sub>). Prior to reduction, the as prepared sample was loaded to the reactor and pre-treated at 300°C for 1h under He flow. The catalyst sample was then cooled in He gas flow to room temperature, before recording the H<sub>2</sub>-TPR trace. Oxygen temperature-programmed desorption was performed (O<sub>2</sub>-TPD) in the same unit. The temperature was increased to 400 °C (heating rate 5 °C/min) under 20 vol% O<sub>2</sub>/N<sub>2</sub> (50 cm<sup>3</sup>/min), for 30 min and were cooled to room temperature to adsorb oxygen for 30 min. After that, the samples were purged under He flow for 1 h, in order to purge physically adsorbed oxygen. The desorption step was conducted under He flow (50 cm<sup>3</sup>/min) up to 750 °C at a rate of 10 °C/min and the signal of O<sub>2</sub> (m/z = 32) were detected by the mass spectrometer.

The catalytic combustion of CH<sub>4</sub> was performed in a fixed-bed reactor loaded with 0.6 g of catalyst. The total gas flow rate was 900cm<sup>3</sup>/min, corresponding to a gas hourly space velocity (GHSV) of ~40,000 h<sup>−1</sup>. The composition of the feed was 0.5 vol% CH<sub>4</sub> and 10 vol% O<sub>2</sub>, balanced with He.

The effect of GHSV was also investigated at 40,000, 20,000, and 10,000 h<sup>-1</sup>. The CH<sub>4</sub> conversion was monitored in the 300–600 °C range (in a decreasing temperature mode) and was held constant at each temperature for ~20 min prior taking measurements. The composition of the effluent gas from the reactor was analysed using gas chromatography (GC-FID, Agilent 7890, Walborn, Germany). Stability of optimum catalyst's performance (time-on-stream) was tested at 600 °C for 10 h (under 0.5 vol% CH<sub>4</sub>, 10 vol% O<sub>2</sub> in He flow). In addition, the effect of H<sub>2</sub>O content (0, 5, and 10% vol. H<sub>2</sub>O in He) was studied on CH<sub>4</sub> oxidation efficiency.

#### 4. Conclusions

Various novel Co-Ce catalysts were prepared following different preparation techniques for the synthesis of ceria support (precipitation or hydrothermal method) and incorporating different loadings of Co on either support. The synthesis route results in ceria carriers of different physicochemical properties, further modified after Co incorporation. Hydrothermal synthesis leads to an improved CeO<sub>2</sub> support, with smaller crystallite size, larger surface area and enhanced reducibility. The ceria support and, thus, the synthetic procedure is important in terms of dispersing the active Co component (smaller Co<sub>3</sub>O<sub>4</sub> crystallites formed on the CeO<sub>2</sub>-H support) and exhibiting higher oxygen mobility (O<sub>2</sub> desorption peak of larger area, additionally appearing at lower temperature), as deduced by comparing the 15Co/CeO<sub>2</sub>-H and 15Co/CeO<sub>2</sub>-P catalytic samples. In summary, a nanocomposite catalyst Co<sub>3</sub>O<sub>4</sub>/CeO<sub>2</sub>-H exhibits higher activity in complete oxidation of CH<sub>4</sub>, than Co<sub>3</sub>O<sub>4</sub>/CeO<sub>2</sub>-P and pure CeO<sub>2</sub> materials. The higher dispersion of the deposited Co species and the enhanced reducibility of Co-Ce catalysts advocate synergistic effects of CeO<sub>2</sub> nanorods and the supported Co<sub>3</sub>O<sub>4</sub> nanoparticles. Moreover, the addition of water vapor in the reaction stream only slightly inhibited the catalytic activity of the optimum selected 15Co/CeO<sub>2</sub>-H catalyst, a fact mainly observed at lower temperature ranges. Thus, the corresponding material is very promising for methane oxidation purposes, as it additionally presented good water resistance properties in wet CH<sub>4</sub> combustion.

**Author Contributions:** The experimental work was conceptualized and designed by E.P. and E.I.; S.D. and E.P. synthesized all catalytic materials, while S.D. helped in performing the evaluation tests and E.P. helped in characterization studies; A.L. provided all resources, while E.P. and E.I. analyzed all experimental results and wrote the original draft. The manuscript was amended and supplemented by all authors. All authors have given approval for the final version of the manuscript.

**Funding:** This research received no external funding.

**Acknowledgments:** The authors would like to thank Ioannis Tsiaousis for performing the HR-TEM characterization.

**Conflicts of Interest:** The authors declare no conflict of interest.

#### References

1. Clark, N.N.; Johnson, D.R.; McKain, D.L.; Wayne, W.S.; Li, H.; Rudek, J.; Mongold, R.A.; Sandoval, C.; Covington, A.N.; Hailer, J.T. Future methane emissions from the heavy-duty natural gas transportation sector for stasis, high, medium, and low scenarios in 2035. *J. Air Waste Manag.* **2017**, *67*, 1328–1341. [[CrossRef](#)] [[PubMed](#)]
2. Farrauto, R.J. Chemistry. Low-temperature oxidation of methane. *Science* **2012**, *337*, 659–660. [[CrossRef](#)] [[PubMed](#)]
3. G elin, P.; Primet, M. Complete oxidation of methane at low temperature over noble metal based catalysts: A review. *Appl. Catal. B* **2002**, *39*, 1–37. [[CrossRef](#)]
4. Filip, M.; Todorova, S.; Shopska, M.; Ciobanu, M.; Papa, F.; Somacescu, S.; Munteanu, C.; Parvulescu, V. Effects of Ti loading on activity and redox behavior of metals in PtCeTi/KIT-6 catalysts for CH<sub>4</sub> and CO oxidation. *Catal. Today* **2018**, *306*, 138–144. [[CrossRef](#)]
5. Chen, J.; Arandiyana, H.; Gao, X.; Li, J. Recent Advances in Catalysts for Methane Combustion. *Catal. Surv. Asia* **2015**, *19*, 140–171. [[CrossRef](#)]

6. Liu, Y.; Deng, J.; Xie, S.; Wang, Z.; Dai, H. Catalytic removal of volatile organic compounds using ordered porous transition metal oxide and supported noble metal catalysts. *Chin. J. Catal.* **2016**, *37*, 1193–1205. [[CrossRef](#)]
7. Dou, J.; Tang, Y.; Nie, L.; Andolina, C.M.; Zhang, X.; House, S.; Li, Y.; Yang, J.; Tao, F. Complete oxidation of methane on  $\text{Co}_3\text{O}_4/\text{CeO}_2$  nanocomposite: A synergic effect. *Catal. Today* **2018**, *311*, 48–55. [[CrossRef](#)]
8. Hu, L.; Peng, Q.; Li, Y. Selective Synthesis of  $\text{Co}_3\text{O}_4$  Nanocrystal with Different Shape and Crystal Plane Effect on Catalytic Property for Methane Combustion. *J. Am. Chem. Soc.* **2008**, *130*, 16136–16137. [[CrossRef](#)] [[PubMed](#)]
9. Jia, Y.; Wang, S.; Lu, J.; Luo, M. Effect of structural properties of mesoporous  $\text{Co}_3\text{O}_4$  catalysts on methane combustion. *Chem. Res. Chin. Univ.* **2016**, *32*, 808–811. [[CrossRef](#)]
10. Teng, F.; Chen, M.D.; Li, G.Q.; Teng, Y.; Xu, T.G.; Hang, Y.C.; Yao, W.Q.; Santhanagopalan, S.; Meng, D.D.; Zhu, Y.F. High combustion activity of  $\text{CH}_4$  and cataluminescence properties of CO oxidation over porous  $\text{Co}_3\text{O}_4$  nanorods. *Appl. Catal. B* **2011**, *110*, 133–140. [[CrossRef](#)]
11. Wang, F.; Zhang, L.; Xu, L.; Deng, Z.; Shi, W. Low temperature CO oxidation and  $\text{CH}_4$  combustion over  $\text{Co}_3\text{O}_4$  nanosheets. *Fuel* **2017**, *203*, 419–429. [[CrossRef](#)]
12. Choi, H.J.; Moon, J.; Shim, H.B.; Han, K.S.; Lee, E.G.; Jung, K.D. Preparation of Nanocrystalline  $\text{CeO}_2$  by the Precipitation Method and Its Improved Methane Oxidation Activity. *J. Am. Ceram. Soc.* **2006**, *89*, 343–345. [[CrossRef](#)]
13. Nabih, N.; Schiller, R.; Lieberwirth, I.; Kockrick, E.; Frind, R.; Kaskel, S.; Weiss, C.K.; Landfester, K. Mesoporous  $\text{CeO}_2$  nanoparticles synthesized by an inverse miniemulsion technique and their catalytic properties in methane oxidation. *Nanotechnology* **2011**, *22*, 135606. [[CrossRef](#)] [[PubMed](#)]
14. Qiao, D.; Lu, G.; Guo, Y.; Wang, Y.; Guo, Y. Effect of water vapor on the CO and  $\text{CH}_4$  catalytic oxidation over  $\text{CeO}_2\text{-MO}_x$  (M = Cu, Mn, Fe, Co, and Ni) mixed oxide. *J. Rare Earths* **2010**, *28*, 742. [[CrossRef](#)]
15. Shi, L.M.; Chu, W.; Qu, F.F.; Hu, J.Y.; Li, M.M. Catalytic performance for methane combustion of supported Mn-Ce mixed oxides. *J. Rare Earths* **2008**, *26*, 836. [[CrossRef](#)]
16. Li, Y.; Guo, Y.; Xue, B. Catalytic combustion of methane over M (Ni, Co, Cu) supported on ceria–magnesia. *Fuel Process. Technol.* **2009**, *90*, 652. [[CrossRef](#)]
17. Liotta, L.F.; Carlo, G.D.; Pantaleo, G.; Deganello, G.  $\text{Co}_3\text{O}_4/\text{CeO}_2$  and  $\text{Co}_3\text{O}_4/\text{CeO}_2\text{-ZrO}_2$  composite catalysts for methane combustion: Correlation between morphology reduction properties and catalytic activity. *Catal. Commun.* **2005**, *6*, 329. [[CrossRef](#)]
18. Honkanen, M.; Kärkkäinen, M.; Kolli, T.; Heikkinen, O.; Viitanen, V.; Zeng, L.; Jiang, H.; Kallinen, K.; Huuhtanen, M.; Keiski, R.L.; et al. Accelerated deactivation studies of the natural-gas oxidation catalyst—Verifying the role of sulfur and elevated temperature in catalyst aging. *Appl. Catal. B Environ.* **2016**, *182*, 439–448. [[CrossRef](#)]
19. Colussi, S.; Arosio, F.; Montanari, T.; Busca, G.; Groppi, G.; Trovarelli, A. Study of sulfur poisoning on Pd/ $\text{Al}_2\text{O}_3$  and Pd/ $\text{CeO}_2/\text{Al}_2\text{O}_3$  methane combustion catalysts. *Catal. Today* **2010**, *155*, 59–65. [[CrossRef](#)]
20. Monai, M.; Montini, T.; Melchionna, M.; Duchoň, T.; Kús, P.; Chen, C.; Tsud, N.; Nasi, L.; Prince, K.C.; Veltruská, K.; et al. The effect of sulfur dioxide on the activity of hierarchical Pd-based catalysts in methane combustion. *Appl. Catal. B Environ.* **2017**, *202*, 72–83. [[CrossRef](#)]
21. Wilburn, M.S.; Epling, W.S. Sulfur deactivation and regeneration of mono- and bimetallic Pd-Pt methane oxidation catalysts. *Appl. Catal. B Environ.* **2017**, *206*, 589–598. [[CrossRef](#)]
22. Friberg, I.; Sadokhina, N.; Olsson, L. Complete methane oxidation over Ba modified Pd/ $\text{Al}_2\text{O}_3$ : The effect of water vapor. *Appl. Catal. B Environ.* **2018**, *231*, 242–250. [[CrossRef](#)]
23. Toso, A.; Colussi, S.; Padigapaty, S.; de Leitenburg, C.; Trovarelli, A. High stability and activity of solution combustion synthesized Pd-based catalysts for methane combustion in presence of water. *Appl. Catal. B Environ.* **2018**, *230*, 237–245. [[CrossRef](#)]
24. Yashnik, S.A.; Chesalov, Y.A.; Ishchenko, A.V.; Kaichev, V.V.; Ismagilov, Z.R. Effect of Pt addition on sulfur dioxide and water vapor tolerance of Pd-Mn-hexaaluminate catalysts for high-temperature oxidation of methane. *Appl. Catal. B Environ.* **2017**, *204*, 89–106. [[CrossRef](#)]
25. Liu, F.; Sang, Y.; Ma, H.; Li, Z.; Gao, Z. Nickel oxide as an effective catalyst for catalytic combustion of methane. *J. Nat. Gas Sci. Eng.* **2017**, *41*, 1–6. [[CrossRef](#)]

26. Lykaki, M.; Pachatouridou, E.; Iliopoulou, E.F.; Carabineiro, S.A.C.; Konsolakis, M. Impact of the synthesis parameters on the solid state properties and the CO oxidation performance of ceria nanoparticles. *RSC Adv.* **2017**, *7*, 6160–6169. [[CrossRef](#)]
27. Lykaki, M.; Pachatouridou, E.; Carabineiro, S.A.C.; Iliopoulou, E.; Andriopoulou, C.; Kallithrakas-Kontos, N.; Boghosian, S.; Konsolakis, M. Ceria nanoparticles shape effects on the structural defects and surface chemistry: Implications in CO oxidation by Cu/CeO<sub>2</sub> catalysts. *Appl. Catal. B Environ.* **2018**, *230*, 18–28. [[CrossRef](#)]
28. Konsolakis, M.; Carabineiro, S.A.C.; Marnellos, G.E.; Asad, M.F.; Soares, O.S.G.P.; Pereira, M.F.R.; Órfão, J.J.M.; Figueiredo, J.L. Effect of cobalt loading on the solid state properties and ethyl acetate oxidation performance of cobalt-cerium mixed oxides. *J. Colloid Interf. Sci.* **2017**, *496*, 141–149. [[CrossRef](#)] [[PubMed](#)]
29. Wang, X.; Zhao, S.; Zhang, Y.; Wang, Z.; Feng, J.; Song, S.; Zhang, H. CeO<sub>2</sub> nanowires self-inserted into porous Co<sub>3</sub>O<sub>4</sub> frameworks as high-performance “noble metal free” hetero-catalysts. *Chem. Sci.* **2016**, *7*, 1109–1114. [[CrossRef](#)] [[PubMed](#)]
30. Xue, L.; Zhang, C.; He, H.; Teraoka, Y. Catalytic decomposition of N<sub>2</sub>O over CeO<sub>2</sub> promoted Co<sub>3</sub>O<sub>4</sub> spinel catalyst. *Appl. Catal. B Environ.* **2007**, *75*, 167–174. [[CrossRef](#)]
31. Bai, B.; Arandiyán, H.; Li, J. Comparison of the performance for oxidation of formaldehyde on nano-Co<sub>3</sub>O<sub>4</sub>, 2D-Co<sub>3</sub>O<sub>4</sub>, and 3D-Co<sub>3</sub>O<sub>4</sub> catalysts. *Appl. Catal. B Environ.* **2013**, *142–143*, 677–683. [[CrossRef](#)]
32. Lou, Y.; Ma, J.; Cao, X.; Wang, L.; Dai, Q.; Zhao, Z. Promoting Effects of In<sub>2</sub>O<sub>3</sub> on Co<sub>3</sub>O<sub>4</sub> for CO Oxidation: Tuning O<sub>2</sub> Activation and CO Adsorption Strength Simultaneously. *ACS Catal.* **2014**, *4*, 4143–4152. [[CrossRef](#)]
33. Sun, Y.; Liu, J.; Song, J.; Huang, S.; Yang, N.; Zhang, J. Exploring the Effect of Co<sub>3</sub>O<sub>4</sub> Nanocatalysts with Different Dimensional Architectures on Methane Combustion. *ChemCatChem* **2016**, *8*, 540. [[CrossRef](#)]
34. Hu, L.H.; Peng, Q.; Li, Y.D. Low-temperature CH<sub>4</sub> Catalytic Combustion over Pd Catalyst Supported on Co<sub>3</sub>O<sub>4</sub> Nanocrystals with Well-Defined Crystal Planes. *ChemCatChem* **2011**, *3*, 868–874. [[CrossRef](#)]
35. Li, Y.; Shen, W. Morphology-dependent nanocatalysts: Rod-shaped oxides. *Chem. Soc. Rev.* **2014**, *43*, 1543–74. [[CrossRef](#)] [[PubMed](#)]
36. Manto, M.J.; Xie, P.; Wang, C. Catalytic Dephosphorylation Using Ceria Nanocrystals. *ACS Catal.* **2017**, *7*, 1931–1938. [[CrossRef](#)]



© 2019 by the authors. Licensee MDPI, Basel, Switzerland. This article is an open access article distributed under the terms and conditions of the Creative Commons Attribution (CC BY) license (<http://creativecommons.org/licenses/by/4.0/>).